Low-Frequency Oscillations in Radiative–Convective Systems. Part II: An Idealized Model

QI HU*

Atmospheric Sciences Research Center, State University of New York at Albany, Albany, New York

DAVID A. RANDALL

Department of Atmospheric Science, Colorado State University, Fort Collins, Colorado

(Manuscript received 25 August 1993, in final form 13 July 1994)

ABSTRACT

A simple model is used to examine the hypothesis that nonlinear interactions among atmospheric radiation, cumulus convection, and the surface moisture flux can result in a stationary, low-frequency (30–60 day period) oscillating heat source in the tropical atmosphere. The model produces low-frequency oscillations of temperature, moisture, and precipitation. The mechanism that produces these oscillations is identified through analyses of the model and its results. The relevance of this mechanism to understanding the observed Madden–Julian oscillation in the tropical atmosphere over the Indian and western Pacific Oceans is discussed.

1. Introduction

In a previous paper (Hu and Randall 1994, hereafter Part I) we presented evidence from one-dimensional numerical models that low-frequency (30–60 day period) oscillations of precipitation, temperature, and moisture can arise spontaneously from nonlinear interactions among atmospheric radiation, cumulus convection, and the surface moisture flux. These interactions include the radiative relaxation process, which couples longwave radiation and temperature, and convective coupling of temperature and moisture. The oscillations are intrinsic to the system and are not forced externally.

In this paper, we extend the previous work from an analytic point of view, in order to provide a conceptual explanation of the three-way interactions among radiation, convection, and surface evaporation, and their roles in the spontaneous, low-frequency oscillations of radiative–convective systems. We use a highly idealized 1D model to pursue this goal.

The physical system represented by the model is the same as that of the two numerical models in Part I and includes the following processes: longwave radiation, cumulus convection, and the surface moisture and sensible heat fluxes. Large-scale dynamics is deliberately omitted. The atmosphere exchanges both mass and energy with the ocean through the lower boundary. The model is nonlinear due to the presence of moist convection. It includes both positive and negative feedbacks.

By studying the model and its behavior, we will address the following questions: 1) How can low-frequency oscillations arise in a radiative–convective system? 2) What conditions favor them? 3) Can the observed low-frequency oscillations in the tropical atmosphere be partially explained by this radiative–convective oscillation?

In the next section, we present the mathematical formulation of the model. The equilibrium solutions and their linear stability are discussed in the first part of section 3. The second part of section 3 presents time-dependent solutions of the nonlinear model. The mechanism of the oscillations is discussed in section 4. Section 5 gives our conclusions.

2. The model

a. Basic framework

As in Part I, the atmosphere is assumed to be horizontally homogeneous over an ocean with fixed sea surface temperature (SST). The pressure at the sea surface is fixed at $p = p_0$. Figure 1 shows the vertical structure of the model. There are two subdomains: a well-mixed boundary layer and a stratified free atmosphere. The mixed layer, with assumed constant depth $\Delta p_M (= p_0 - p_B)$, is characterized by vertically uniform dry static energy s_M and mixing ratio q_M. Across the top of the mixed layer is the free atmosphere, which extents from p_B to p_T. In the free atmosphere, we as-

* Current affiliation: Pacific Northwest Laboratories, Richland, Washington.

Corresponding author address: Dr. Qi Hu, Pacific Northwest Laboratories, K9-37, P.O. Box 999, Richland, WA 99352.

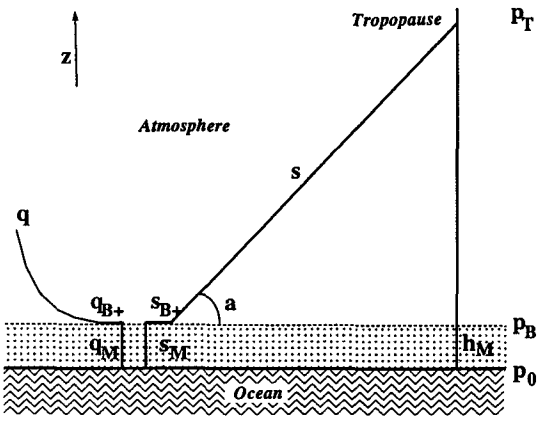

FIG. 1. Schematic structure of the model. The atmosphere is over a uniform ocean surface and is composed of two subdomains: a well-mixed boundary layer, from p_0 to p_B, and a stratified free atmosphere, from p_B to p_T. See text for other details.

sume a dry static energy profile that is linear with pressure; that is,

$$s(p, t) = s_{B^+}(t) + a(t)\eta(p), \tag{1}$$

where the slope, $a(t)$, is defined as

$$a(t) \equiv \frac{\partial s(p, t)}{\partial p} = \frac{s_T - s_{B^+}}{p_T - p_B} \leqslant 0, \tag{2}$$

and

$$\eta(p) \equiv p - p_B \leqslant 0.$$

In the above, the subscript B^+ denotes a level just above the top of the mixed layer. The dry static energy s is defined as $s = c_pT + gz$, where c_p is specific heat at constant pressure, T is temperature, g the gravitational acceleration, and z the height. The mixing ratio in the free atmosphere is assumed to decrease exponentially upward with pressure; that is,

$$q(p, t) = q_{B^+}(t) \exp\left[\frac{\eta(p)}{P_q}\right], \tag{3}$$

where P_q denotes the pressure scale depth for moisture.

As shown in Fig. 1, p_T is the level where the two curves h_M = const and $s(p, t)$ intersect. Here, the mixed-layer moist static energy h_M is defined as $h_M = s_M + Lq_M$. We assume that p_T is a constant. Our model says nothing about the sounding for $p < p_T$. Since $q_T \approx 0$, we have, at $p = p_T$,

$$h(p_T) = s(p_T) = h_M. \tag{4}$$

With assistance from this relation we can rewrite (2) as

$$a(t) \approx \frac{s_M + Lq_M - s_{B^+}}{p_T - p_B}, \tag{5}$$

which serves as a diagnostic relation for $a(t)$ in terms of the other model variables.

The physical processes that are responsible for maintaining the thermodynamic and moisture structure presented in Fig. 1 include radiation, moist convection, and the surface moisture and sensible heat fluxes. We use Newtonian cooling to parameterize the radiation term. The fluxes of moisture and sensible heat from the ocean are calculated using the bulk aerodynamic formula with a specified near-surface wind speed $|V_s|$. Moist convection is represented by a single cloud type whose fractional entrainment rate is zero and whose mass flux is independent of height (Arakawa and Schubert 1974). This cloud extends to $p = p_T$, where the neutral buoyancy condition (4) is observed. Moist convective updrafts are assumed to originate in the mixed layer. These physical processes play different parts in the mixed layer and in the free atmosphere and determine the evolution of s and q in these portions of the atmosphere.

In the mixed layer, the change of dry static energy is affected by all three processes. The time change of s_M can be written as

$$\frac{\partial s_M}{\partial t} = \frac{gF_{s_0}}{\Delta p_M} - \frac{s_M - s_{R_M}}{\tau} + gM_c\frac{s_{B^+} - s_M}{\Delta p_M}, \tag{6}$$

where

$$F_{s_0} = \rho_0 c_D |V_s|(s_{00} - s_M) \tag{7}$$

is the flux of dry static energy from the surface. In the above, ρ_0 is the air density at the sea level, c_D is a turbulent transfer coefficient, $|V_s|$ is the surface wind speed, and s_{00} is the dry static energy value at the sea surface temperature. In (6), s_{R_M} corresponds to radiative equilibrium value of s in the mixed layer, assumed to be constant, and τ is the radiative relaxation timescale, also assumed to be constant. The symbol M_c, in the third term on the right-hand side of (6), is the convective mass flux, which measures intensity of convection, and is parameterized by a method described in section 2b.

The time change of s in the free atmosphere, in the absence of large-scale dynamics, is influenced by radiation and moist convection. The surface fluxes have no direct influence on it. This time change can be written as

$$\frac{\partial s}{\partial t} = -\frac{s - s_R}{\tau} - gM_c\frac{\partial s}{\partial p} - D, \quad p_{B^+} \geqslant p \geqslant p_T, \tag{8}$$

where s_R is the radiative equilibrium profile of s, which is assumed to have a linear form with pressure; that is,

$$s_R(p) = s_{R_B} + a_R\eta(p). \tag{9}$$

Here s_{R_B} is the value of s_R at p_{B^+} and is specified; and a_R is the slope of s_R in the free atmosphere. The second and the third terms on the rhs of (8) account for the effects of convection. In particular, the second term

describes subsidence warming, and the third accounts for the effects of detrainment. As there is only one type of cumulus cloud in the model, and this cloud only detrains at $p = p_T$, the influence of detrainment on s in the free atmosphere, where s maintains a linear profile, is assumed to be uniformly distributed in the vertical. The form of D is determined by imposing conservation of dry static energy (see appendix A), after assuming that the precipitation satisfies

$$P_r = cq_M M_c. \tag{10}$$

Here the parameter c measures the precipitating fraction of the convective moisture flux. When (8) is applied at $p = p_{B^+}$ we obtain, after substitution of (A3) for D, a prognostic equation for s_{B^+}:

$$\frac{\partial s_{B^+}}{\partial t} = -\frac{s_{B^+} - s_{R_B}}{\tau} - gM_c a - \frac{g(1-c)}{(p_B - p_T)} Lq_M M_c. \tag{11}$$

Moisture variations are produced only by moist convection and the surface moisture flux. The conservation of moisture in the mixed layer can be written as

$$\frac{\partial q_M}{\partial t} = \frac{gF_{q_0}}{\Delta p_M} - \frac{gM_c}{\Delta p_M}(q_M - q_{B^+}), \tag{12}$$

where F_{q_0} is the surface moisture flux and is calculated from a formula similar to (7):

$$F_{q_0} = \rho_0 c_D |V_s|(q_{00}^* - q_M).$$

Here q_{00}^* is the saturation mixing ratio at the given SST and sea level pressure. In the free atmosphere, moist convection plays the primary role in evolution of moisture. The moisture change here results from drying due to compensating subsidence motion and from moistening due to evaporation of condensates detrained from convection; it can be expressed by

$$\frac{\partial q}{\partial t} = -gM_c \frac{\partial q}{\partial p} + gM_c K e^{\eta(p)/P_q}, \quad p_{B^+} \geq p \geq p_T. \tag{13}$$

The term involving K on the rhs of (13) is a counterpart of the D term in (8). The form of K is determined by requiring the conservation of total moisture (appendix A). Substituting (A6) for K and applying (3), (13) can be rewritten, when applied at $p = p_{B^+}$, as

$$\frac{\partial q_{B^+}}{\partial t} = [(1-c)q_M - q_{B^+}]gM_c P_q^{-1}. \tag{14}$$

Our model consists of four prognostic equations, (6), (11), (12), and (14), and one diagnostic relation, (5). The model conserves dry static energy and water mass, as well as moist static energy. The model is not closed, however, because M_c is unknown. We next describe a simple cumulus parameterization to determine M_c.

b. *Cumulus parameterization*

The convective mass flux M_c is determined by considering the time change of temperature and moisture, including both the free atmosphere and the mixed layer. An air parcel in the mixed layer can rise into the free atmosphere when it is positively buoyant with respect to its environment. The physical processes that can produce such positive buoyancy include radiation, surface fluxes, and large-scale motions. In this model only the former two are included.

Under the quasi-equilibrium assumption (Arakawa and Schubert 1974), the rates of production and consumption of positive buoyancy by radiation, surface fluxes, and moist convection are such that

$$\frac{dA}{dt} = 0, \tag{15}$$

where A is the cloud work function, an integral measure of the buoyancy available to a lifted parcel. Since A is a function of both convection and large-scale forcing, (15) allows the intensity of moist convection to be determined for given large-scale conditions. In a review article on cumulus parameterization schemes, Arakawa and Chen (1987) showed that (15) can be interpreted in terms of a relationship between temperature and moisture, such that variations of the relative humidity near the surface (RH_s) are negatively correlated with changes in the lapse rate. We base our convection parameterization scheme on this idea. We define a function G by

$$G \equiv \Gamma_N - (1 - \mathrm{RH}_s). \tag{16}$$

Here Γ_N is the normalized lapse rate defined by (Arakawa and Chen 1987)

$$\Gamma_N = \frac{\Gamma - \Gamma_{m_s}}{\Gamma_d - \Gamma_{m_s}}, \tag{17}$$

where $\Gamma = -dT/dz$, $\Gamma_d = g/c_p$, and Γ_{m_s} is the moist-adiabatic lapse rate at the surface. The quasi-equilibrium assumption (15) is essentially equivalent to (Arakawa and Chen 1987)

$$\frac{dG}{dt} = 0. \tag{18}$$

Further, if we write Γ as

$$\Gamma = \frac{s_M - s_{B^+} - a(p_{500} - p_B) + gz_{500}}{c_p z_{500}}, \tag{19}$$

we can rewrite (16) as

$$G = \frac{(1-R)(s_M - s_{B^+}) - (W - LR)q_M}{Wq_{00}^*}. \tag{20}$$

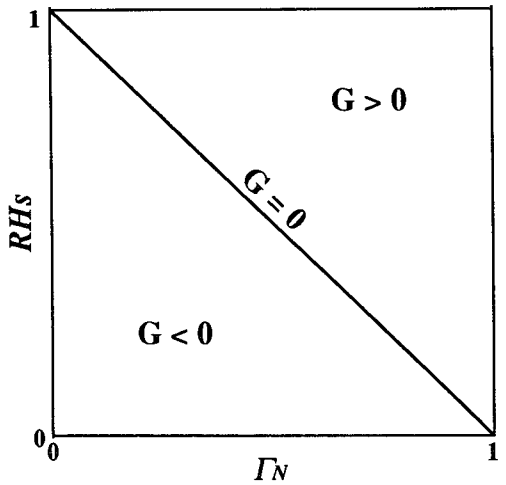

FIG. 2. Distribution of G in the (RH_s, Γ_N) plane.

Here

$$W = \frac{c_p z_{500}(\Gamma_d - \Gamma_{m_s})}{q^*_{00}} \quad \text{and} \quad R = \frac{p_{500} - p_B}{p_T - p_B}.$$

The subscript 500 denotes values at the 500-hPa level. By substituting (20) into (18) and applying the equations derived in the previous subsection, we obtain a relation that links the convective cloud mass flux M_c to the large-scale variables of the model. The particular form of M_c is shown later.

The physical meaning of G becomes clear when we consider the processes that affect it. As shown in Fig. 2, we actually force $G \leq 0$; that is, positive values are not allowed. Such positive values would represent finite convective instability. The function $G = 0$ defines a straight line in the (RH_s, Γ_N) plane. Since radiation and the surface moisture flux act to increase the lapse rate (Manabe and Möller 1961) and the low-level moisture, respectively, both of these processes tend to increase G. From this point of view, the role of G in this model is similar to that of the cloud work function in a more complete model. The restriction on variations of G, that is, (18), determines the convection intensity necessary to maintain quasi equilibrium.

We must require a nonnegative cloud mass flux; that is,

$$M_c \geq 0. \tag{21}$$

When $G < 0$ the atmosphere is convectively stable. In this case a negative M_c would be required to satisfy (18) and force $G = 0$. Because such a negative M_c is physically impossible, we enforce (21).

3. Solutions

a. Linear analysis

The equilibrium solutions of our model are as follows:

$$\bar{s}_{B^+} = \frac{A^{-1}BD + \tau^{-1}s_{R_B} + Lq^*_{00}H^{-1}(D - F)}{(\tau^{-1} + D - A^{-1}CD)},$$

$$\bar{s}_M = \frac{B + C\bar{s}_{B^+}}{A},$$

$$\bar{q}_M = q^*_{00}\left(1 + \frac{c}{v}\bar{M}_c\right)^{-1},$$

$$\bar{q}_{B^+} = q^*_{00}(1 - c)\left(1 + \frac{c}{v}\bar{M}_c\right)^{-1}, \tag{22}$$

where an overbar denotes an equilibrium solution value. The other symbols appearing in (22) are defined in appendix B. The equilibrium solution for the convective mass flux $\bar{M}_c$ is obtained through a procedure similar to that outlined in section 2b. Following this procedure, as shown in appendix C, we can get an algebraic equation of degree four for $\bar{M}_c$. For the parameter values listed in Table 1, it can be shown that there is only one, among the four roots of this equation, that satisfies (21). This solution has the form

$$\bar{M}_c = \left[\left(\frac{s_{R_B}}{\tau} - \frac{q^*_{00}(W - LR)}{\tau(1 - R)}\right)\cdot\left(\frac{gv}{\Delta p_M} + \frac{1}{\tau}\right) - \frac{B}{\tau}\right] \times \left[\frac{cB}{v\tau} - \frac{cs_{R_B}}{v\tau}\left(\frac{gv}{\Delta p_M} + \frac{1}{\tau}\right) + \frac{q^*_{00}(W - LR)}{\tau(1 - R)}\frac{gv}{\Delta p_M} + \frac{gq^*_{00}}{p_B - p_T}\left(\frac{(W - LR)}{(1 - R)} - c\right)\left(\frac{gv}{\Delta p_M} + \frac{1}{\tau}\right)\right]^{-1}. \tag{23}$$

The equilibria, as functions of SST and the surface wind speed in terms of mixed layer mixing ratio $\bar{q}_M$, temperature $\bar{T}_M$, and precipitation rate $\bar{P}_r$, are shown in Fig. 3. The other model parameters are given in Table 1. As shown in Fig. 3a, the mixing ratio in the boundary layer increases quickly when the SST or the surface wind speed increases. The equilibrium value of $\bar{q}_M$ approaches the saturation mixing ratio when the SST is

TABLE 1. Parameters.

Radiation relaxation timescale	τ = 20 days
Surface pressure	p_0 = 1000 hPa
Pressure at the tropopause	p_T = 200 hPa
Pressure thickness of the mixed layer	Δp_M = 200 hPa
Pressure scale for moisture in the free atmosphere	p_q = 100 hPa
Precipitation efficiency factor	c = 0.6
Radiative equilibrium temperature in the mixed layer	T_{R_M} = 288 K
Radiative equilibrium temperature at $p = p_B$	$T_{R_{B^+}}$ = 278 K

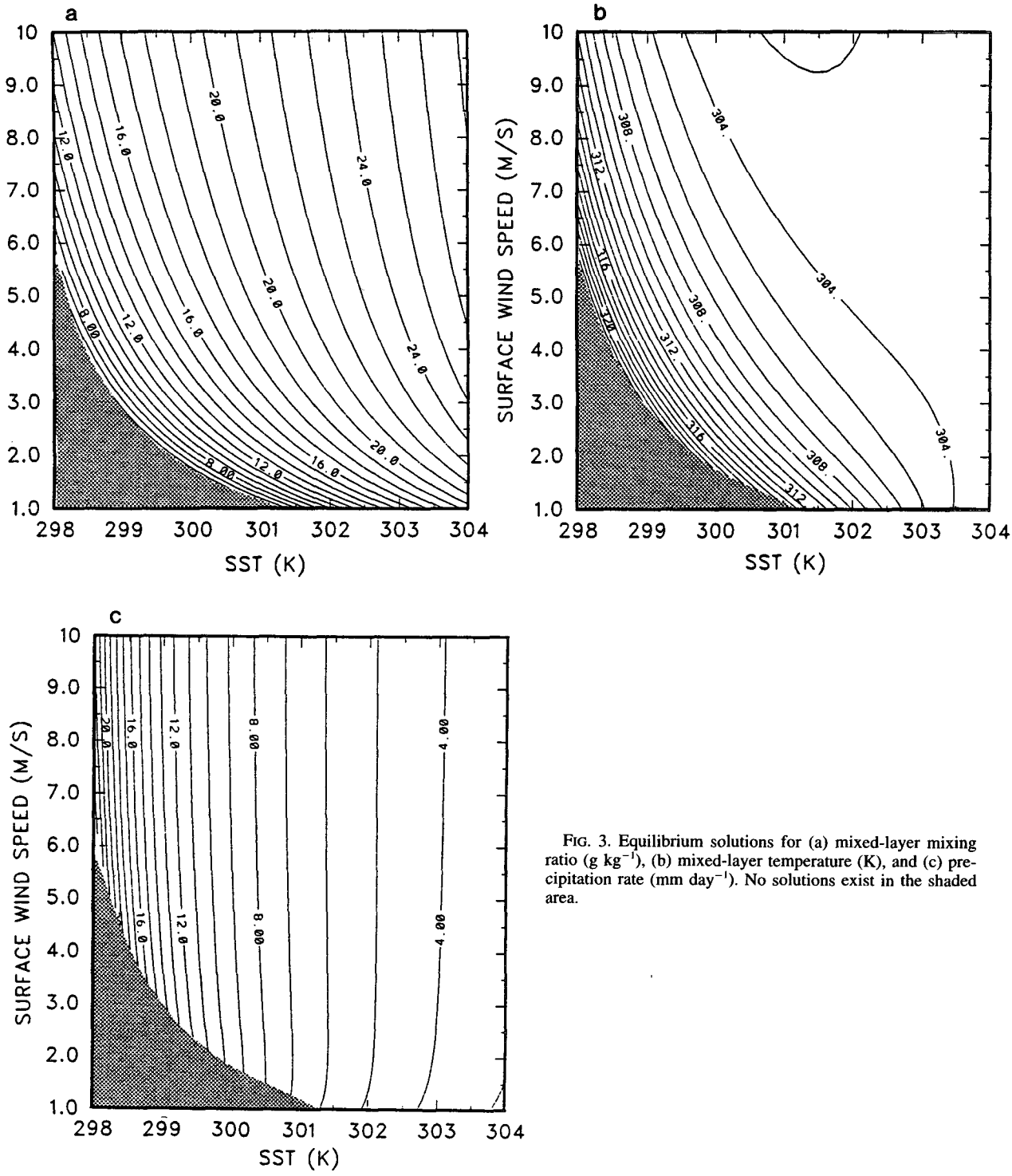

FIG. 3. Equilibrium solutions for (a) mixed-layer mixing ratio (g kg^{-1}), (b) mixed-layer temperature (K), and (c) precipitation rate (mm day^{-1}). No solutions exist in the shaded area.

warmer than 302 K and the surface wind speed is greater than 2 m s^{-1}. The cloud mass flux computed from (23) decreases at high SSTs. This result, which is similar to that discovered by Betts and Ridgway (1989) in their 1D model, is consistent with the behavior of $\bar{q}_M$ at higher SSTs. An interpretation is that $\bar{M}_c \to 0$ when $\bar{q}_M \to q^*_{00}$. This can be easily shown by rewriting the equilibrium solution for $\bar{q}_M$, given in (22), as

$$\bar{M}_c = \frac{v}{c\bar{q}_M}(q_{00}^* - \bar{q}_M). \quad (24)$$

This relation also helps to explain a positive correlation between the surface moisture flux and intensity of convection, as discussed in section 4.

Consistent with the result in Fig. 3a, Fig. 3b shows that $\bar{T}_M$ decreases when SST increases. This is because $\bar{T}_M$ is also strongly influenced by convection, as described in (6). Since $\bar{M}_c$ decreases as SST increases, the compensating subsidence warming weakens, and therefore $\bar{T}_M$ decreases. Weak convective mass flux also results in a decrease in precipitation as shown in Fig. 3c. Our parameterization of the precipitation rate, that is, (10), involves the product of q_M and M_c. The variations of $\bar{q}_M$ and $\bar{P}_r$ as functions of SST (Figs. 3a and 3c) are determined by the decrease of M_c as SST increases.

In the shaded region of Fig. 3, $\bar{M}_c = 0$ and $\bar{G} < 0$. The equilibrium solutions are nonconvective. Since, as we will show in the next subsection, convection is necessary in this model in order to maintain a reasonable vertical thermodynamic structure, these nonconvective solutions are physically impossible. As shown in Fig. 3, the shaded region stretches toward warm SSTs when the surface wind speed becomes small. This indicates that with weak surface winds solutions of the model exist only when the SST is warm enough.

The linear stability of the model when perturbed about the equilibrium solutions is shown in Fig. 4. This figure shows the sign of the largest real part of the four complex eigenvalues of the model. The shaded area, including both the dark and light shaded regions, indicates positive values. An equilibrium solution in this region has at least one growing mode among the four eigenmodes and is therefore unstable. The hatched area indicates where the largest real part of the four eigenvalues is zero or negative. All modes in the hatched area are either neutral or damped.

The imaginary parts of the eigenvalues, whose real parts are shown in the unstable region in Fig. 4, are all zero (not shown). This implies that, from the point of view of linear theory, the most rapidly growing mode is nonoscillatory. In the stable region of Fig. 4, the corresponding imaginary parts have complicated structures, but in general they are all very small [$\leq O(10^{-8})$].

These results from linear stability analysis show the behavior of only the gravest linear mode as a function of SST and the surface wind speed. This gravest linear mode is the most important mode in the linear sense, as it dominates the model's linear behavior. This linear analysis cannot reveal the nature of a nonlinear system, however. Nonlinear analyses, for example, bifurcation analysis and/or numerical solutions to the fully nonlinear model system, are capable of describing the nonlinear behavior of the system. Due to the mathematical difficulty imposed by the nonnegative convective mass flux, a rigorous bifurcation analysis has not been performed. In the following, we analyze the solutions obtained by numerical integrations of the fully nonlinear system, in order to understand the nonlinear behavior of the system.

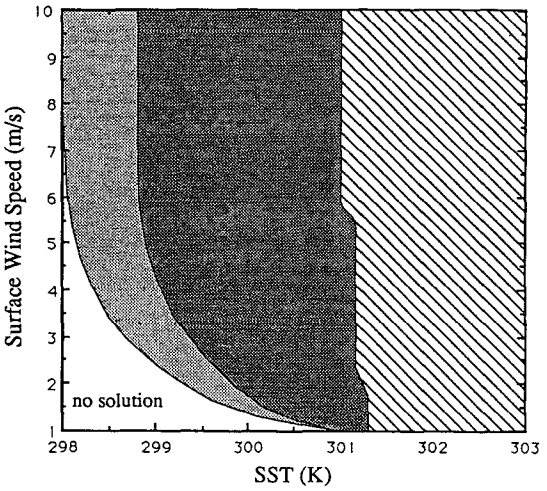

FIG. 4. Stability of the gravest linear mode. The mode has a positive real part in the shaded area (including both dark and light shaded regions), and a zero or negative real part in the hatched region.

b. Numerical solutions of the nonlinear model

The system of equations to be numerically integrated consists of (5), (6), (11), (12), and (14), subject to (18) and (22). The prognostic variables at each new time level are predicted using a simple forward time-stepping method.

Because the intensity of convection during a time step is determined by large-scale processes on the same time step, a set of provisional values of the prognostic variables is calculated by assuming $M_c = 0$. From these values we calculate a provisional value for the function G. A positive provisional value of G indicates that moist convection is required on that time step in order to maintain the quasi-equilibrium condition. In this case the convective mass flux is computed from (18), and the provisional values are corrected. On the other hand, if G is either zero or negative, no convection is needed and the provisional values are accepted as the new, updated values. A detailed description of this procedure is given by Hu (1992).

The nonlinear model has been integrated in 1000-day runs, with a time step of 30 minutes. The results presented here are taken from the second 500 days of these 1000-day integrations. The numerical values of some of the parameters used in the integrations are listed in Table 1. These values are used unless stated otherwise.

In the interesting range of SST and surface wind speed, that is, 298 K $\leq$ SST $\leq$ 303 K and 1 m s^{-1} $\leq |V_s| \leq$ 10 m s^{-1}, three different types of solutions

have been found. We obtain steady solutions when SST and $|V_s|$ correspond to a solution in the stable region in Fig. 4. These solutions are identical to the equilibria discussed earlier. When the SST and $|V_s|$ correspond to a solution in the unstable region of Fig. 4, two types of solutions can occur depending on whether the solution is in the light or dark shaded region. (The boundary separating the dark shaded region from the rest of the unstable region in Fig. 4 is sketched based on numerical experiments. An accurate specification of this boundary should be based on bifurcation analysis.) In the dark shaded region, solutions are oscillations and physically reasonable. In the light shaded region, the solutions turn out to be physically impossible. These solutions are characterized by either negative mixing ratio values, more often for q_{B^+}, or by unrealistically large values of the dry static energy.

These physically impossible solutions indicate that the model is unable to describe the atmosphere when the SST is cold (the light shaded region has the lowest SSTs in Fig. 4). This limitation seems to be a consequence of the fact that the assumed thermodynamic profiles in the model (Fig. 1) are reasonable only over warm SSTs, particularly when large-scale dynamics is neglected. Omission of large-scale dynamics demands a nonzero daily precipitation in order to maintain reasonable thermodynamic and moisture profiles in the model. This has been indicated by a nonzero precipitation rate in the equilibrium solutions of this model. Continuous precipitation was also obtained in the numerical models in Part I and in other 1D radiative–convective models (e.g., Satoh and Hayashi 1992). Because precipitation is difficult to maintain over a cool ocean surface, realistic solutions are restricted to warm SSTs. Observations (e.g., Waliser and Graham 1993) have shown that in the Tropics deep convection rarely occurs when the SST is below 299 K. Similarly, because a very weak surface wind speed cannot support evaporation, the model is restricted to relatively strong surface wind speeds (≥ 1 m s^{-1}). Although deep convection in the Tropics is not observed to be continuous in time, the thermodynamic profiles and the processes described by this model are physically self-consistent for conditions of warm SST and relatively strong surface wind.

Figure 5 shows examples of the oscillations. In this figure we plot the evolution of daily perturbation precipitation, subject to a Fourier analysis that removes all periods shorter than or equal to 5 days. Figure 5a shows a case with SST = 300 K and $|V_s| = 4$ m s^{-1}. Figure 5b is for the same SST but $|V_s| = 8$ m s^{-1}. The other parameter values used in these integrations are given in Table 1. The averaged values of the daily precipitation in these two cases are equal to their equilibrium values as given in Fig. 4.

The oscillation in Fig. 5a shows double periods. The longer one is around 75 days and the shorter one is about 15 days. In Fig. 5b the outstanding period is

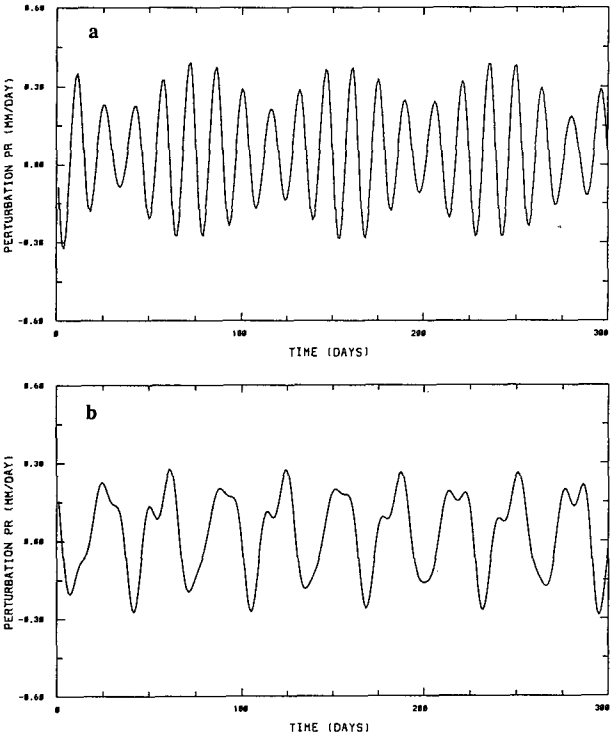

FIG. 5. Evolution of daily perturbation precipitation when SST = 300 K and (a) $|V_s| = 4$ m s^{-1}, and (b) $|V_s| = 8$ m s^{-1}. Other parameters used are as given in Table 1.

about 30 days. The amplitude of the oscillations in this case is a little smaller than that in Fig. 5a. The weakening of the oscillation with an increase of the surface wind speed becomes significant when the SST is close to 301 K. This is illustrated by the difference between the two panels in Fig. 6. The results in this figure were obtained for SST = 300.5 K; the surface wind speed used in the upper panel is 5 m s^{-1}, and for the lower panel it is 8 m s^{-1}.

When the SST increases from a point in the dark shaded region in Fig. 4 to a point near the stable region, the oscillation's amplitude decreases. This is shown in Figs. 5b and 6b. The same surface wind value was used for both figures, but for Fig. 6b the SST was 300.5 K, while for Fig. 6a it was 300 K. When the SST takes a value inside the stable region in Fig. 4, the oscillation does not appear.

Studies of the sensitivity of the oscillations to the radiation relaxation timescale τ show that low-frequency oscillations are maximized when τ is close to 20 days. When τ decreases, the amplitude of the oscillations decreases. Figure 7 shows a result for $\tau = 10$ days, SST = 300.5 K, and $|V_s| = 5$ m s^{-1}. Compared to the result in Fig. 6a, the amplitude of the oscillation is much smaller and the frequency is higher. Tests with larger values of τ, for example, $\tau = 30$ days or longer, also produced small-amplitude oscillations (not shown).

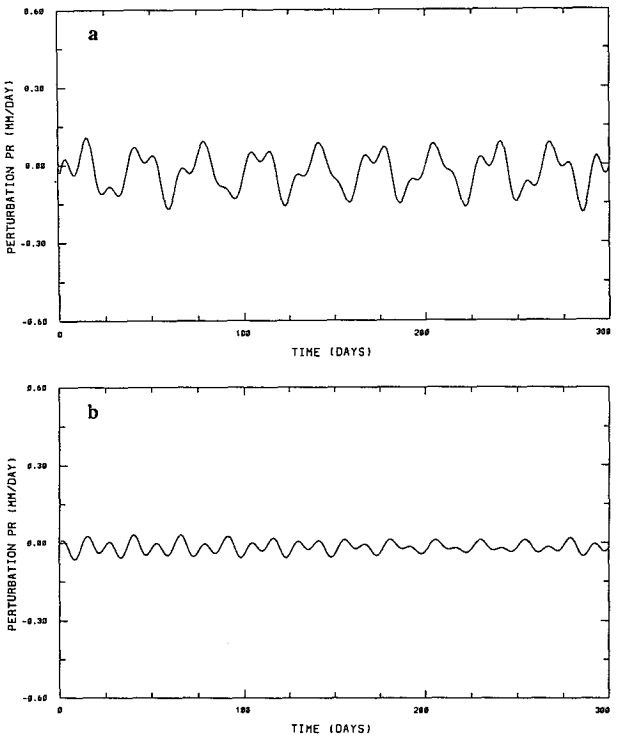

FIG. 6. As in Fig. 5 but for SST = 300.5 K and (a) $|V_s| = 5$ m s^{-1}, and (b) $|V_s| = 8$ m s^{-1}.

In studies of the sensitivity of the solutions to the other parameters we found that, within the reasonable range of model parameters given in Table 2, low-frequency oscillations always occur. The low-frequency oscillation is a robust phenomenon of this model in the physically reasonable range of model parameter values. The sensitivity of the period and amplitude of these oscillations to model parameters is similar to that discussed in the above and illustrated in Figs. 5–7. In the following, we will discuss the details of one of these oscillations and compare them with the oscillations discussed in Part I.

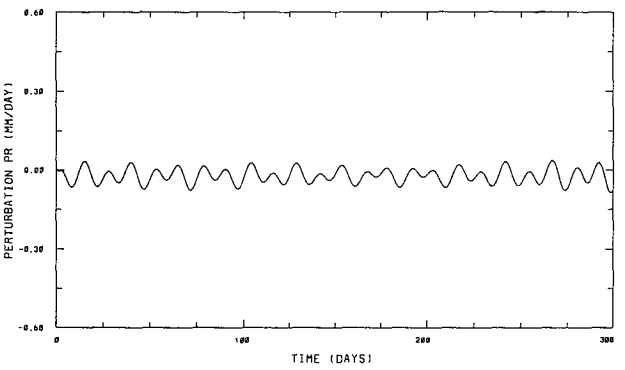

FIG. 7. Evolutions of daily perturbation precipitation when $\tau = 10$ days, SST = 300.5 K, and $|V_s| = 5$ m s^{-1}. Other parameters used are as given in Table 1.

TABLE 2. Parameter variation range in sensitivity tests.

Parameters	Variation range in test
Pressure at the tropopause	100–300 hPa
Pressure thickness of the mixed layer	100–200 hPa
Pressure scale for moisture in the free atmosphere	100–150 hPa
Precipitation efficiency factor	0.5–0.7
Radiative equilibrium temperature in the mixed layer	278–295 K
Radiative equilibrium temperature at $p = p_B$	272–288 K

Figure 8 shows an example of an oscillating solution. In this case, SST = 300.4 K and the surface wind speed

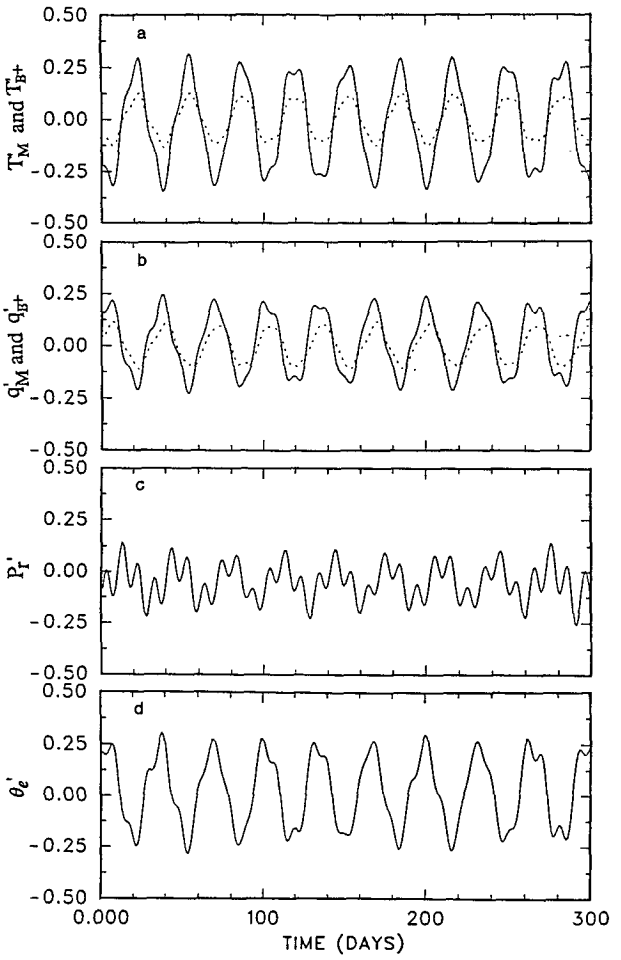

FIG. 8. An integration result showing variations of (a) perturbation temperature in the mixed layer (solid) and at $p = p_B$ (dashed) (K); (b) as (a) but for mixing ratio (g kg^{-1}); (c) perturbation precipitation rate (mm day^{-1}); and (d) perturbation equivalent potential temperature in the mixed layer (K).

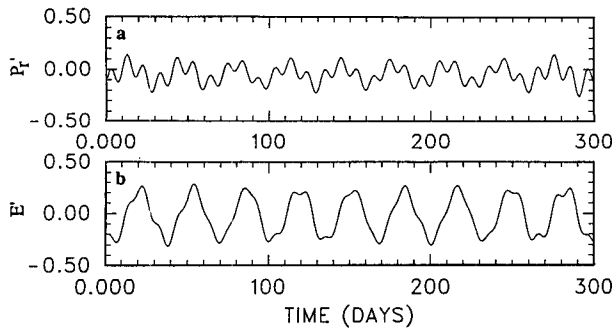

FIG. 9. Variations of (a) perturbation precipitation rate (mm day^{-1}) and (b) the surface evaporation rate (mm day^{-1}).

is 4 m s^{-1}. Fluctuations with periods shorter than 5 days were filtered before plotting. The top panel shows the perturbation temperature. The solid line is for T'_M and the dashed line for T'_{B^+}. The second panel shows the perturbation moisture in the mixed layer (solid line) and at $p = p_{B^+}$ (dashed line). Panel c shows the perturbation precipitation. The mean values of T_M, T_{B^+}, q_M, q_{B^+}, and the precipitation are, respectively, 306 K, 303 K, 16.9 g kg^{-1}, 3.0 g kg^{-1}, and 7.6 mm day^{-1}, and are identical to their equilibrium values (see Fig. 4). The perturbation equivalent potential temperature in the mixed layer, θ_{e_s}, is also plotted (panel d). An oscillation of period 35–40 days is obvious.

As shown in Fig. 8, the variation of θ_{e_s} shows an in-phase relation with that of q_M. The variation of θ_{e_s} leads that of precipitation. For example, the precipitation rate always intensifies shortly after θ_{e_s} reaches its maximum. Following the increase in precipitation, θ_{e_s} decreases. Cumulus convection remains weak as long as θ_{e_s} is low.

The time evolution of model states in the (RH$_s$, Γ_N) plane, during the oscillation, shows movement along the $G = 0$ line, back and forth with a reversal of direction every 15–20 days (refer to Fig. 10b).

The oscillations produced by this highly idealized model resemble in many ways those produced by the more complicated numerical models discussed in Part I. For example, a positive correlation between precipitation and the surface evaporation is present in this model. As shown in Fig. 9, a local maximum in the surface evaporation always occurs shortly after a local maximum in precipitation. The subsequent moistening of the mixed layer, under weak convection, leads to another episode of intense convection. We will further discuss this in the next section.

There are also differences in the temperature and moisture variations between the results of this model and those of the earlier models. The mixed-layer temperature, for example, varies in an out-of-phase relation with the mixed-layer specific humidity (e.g., Figs. 8a and 8b).

The presence of similar low-frequency oscillations in all three of these very different models indicates that the features shared in common by all these models, that is, the accumulation of moisture in the mixed layer and the variation of the lapse rate, governed by both convection and radiation, are essential for the low-frequency oscillations.

4. The mechanism of the oscillation

Figure 10 shows the details of one cycle of the oscillations presented in Fig. 8. The upper panel shows the variation of perturbation mixing ratio in the mixed layer, and the lower panel plots the model states in the (RH$_s$, Γ_N) plane for the five selected times marked in Fig. 10a, that is, A through E. As Fig. 10b shows, the model undergoes a back-and-forth movement along the $G = 0$ line. The atmosphere changes from a condition of dry mixed layer and steep lapse rate to a moisture-rich mixed layer with a less steep temperature profile, and repeats.

The mechanism behind the oscillation in the model is schematically illustrated in Fig. 11. The tendencies due to the physical processes in the model, including radiation, the surface moisture flux, and moist convection, are represented by arrows in this figure. For a model state at the center of the (RH$_s$, Γ_N) plane, radiation tends to pull the state to a steep or unstable lapse rate (Manabe and Möller 1961) or to the right-hand

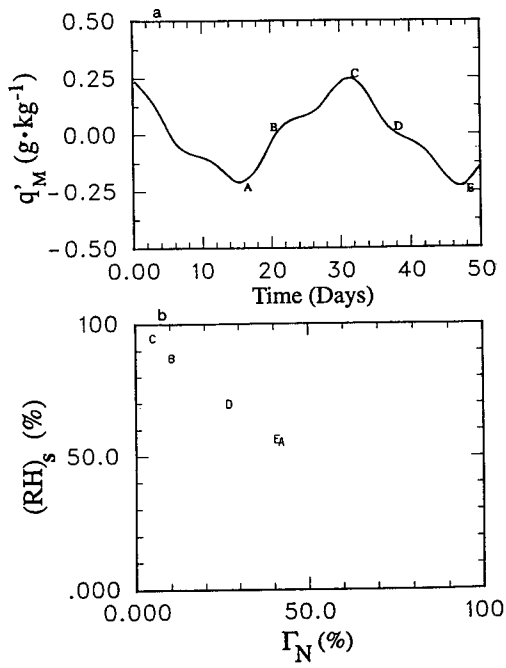

FIG. 10. (a) A segment of the variations from Fig. 8 showing the oscillation of the mixing ratio in the model boundary layer. (b) The corresponding variation of model state in the (RH$_s$, Γ_N) plane during the oscillation.

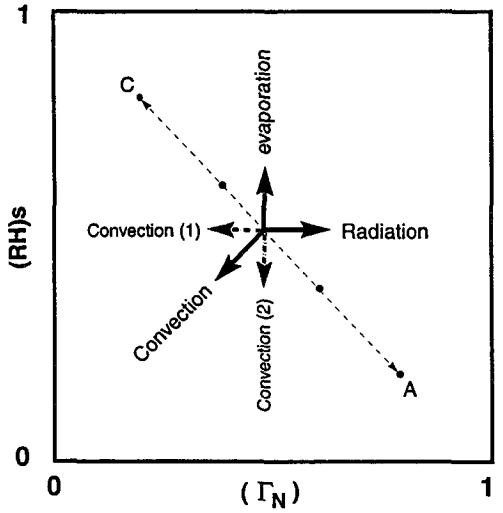

FIG. 11. Schematic summary of the interactions among radiation, cumulus convection, and the surface moisture flux.

side of the picture. The surface moisture flux tends to moisten the mixed layer and therefore pushes the model state up to high RH_s values. A measure of the intensity of a forcing is the distance away from the boundary toward which the forcing drives the system.

As radiation and the surface moisture flux tend to drive the model toward the region with $G > 0$, they destabilize the model atmosphere. A neutral state is maintained by convection, whose net effect is to drive the model toward $G < 0$ by simultaneously changing both the mixed-layer moisture (denoted by Convection 2 in Fig. 11, hereafter C2) and the lapse rate (denoted by Convection 1 in Fig. 11, hereafter C1).

An oscillation, rather than a steady state, is chosen due to nonlinear interactions among the three physical processes, whose timescales are vastly different. When a model state is at A in Fig. 11, it experiences mainly the forces from surface evaporation and convection. The major role of convection at this stage is to change the lapse rate in response to the addition of moisture to the atmosphere through moisture flux (process C1). At this time the mixed layer is dry and has the potential for moistening. A dry mixed layer is also unfavorable for intense convection, and so convection is weak.

While the surface flux raises the mixed-layer moisture, weak moist convection continuously depletes a portion of the moisture via precipitation and meanwhile transports some of the mixed layer's moisture to the upper part of the atmosphere (see Fig. 10). It is easy to show that when this drying of the mixed layer by convection is neglected, it takes about one week for the surface moisture flux to raise the relative humidity of a mixed layer 200 hPa thick from 50% to 90%, with a surface wind speed at 5 m s^{-1} and an SST of 300 K. This timescale is lengthened when drying by convection is taken into account. In addition, the warming and drying due to the subsidence motion to the mixed layer also help to prolong this timescale. As a result, it takes more than 15 days, in this particular case, for the moisture flux to increase the mixed layer relative humidity to the value corresponding to C in Fig. 11.

State C in Fig. 11 is characterized by a moist atmosphere with a small lapse rate. High relative humidity in the mixed layer suppresses the surface evaporation. The small lapse rate enhances radiative cooling (Paltridge and Platt 1976). At C, the dominant forcing changes. The forcing now is mainly due to radiation, which tries to steepen the lapse rate, and the role of convection changes to drying the atmosphere in response to the lapse rate change by radiation (C2).

When the model state is near the position C in Fig. 11, convection peaks in intensity and precipitation is strong. This is a consequence of abundant moisture and strong radiative destabilization.

The timescale for the model to move from state C back to state A is determined mainly by radiation relaxation process and by convective coupling of changes in temperature and moisture. When radiation is steepening the lapse rate of a moist atmosphere it is necessary for intense convection to dry the moisture profile to be compatible with the changes in temperature. The convective warming counteracts the cooling by radiation, and meanwhile convection promotes surface evaporation by reducing the mixed layer's humidity. These interactions act to slow down the relaxation process dominated by radiation and prolong its timescale on the order of a few tens of days. For the case presented in Fig. 10, it takes about 20 days for the model to "relax" from C to A.

When the model arrives at A, the major forcing changes back to the surface evaporation and the convective process C1. The dominant forcing on the model shifts between radiation/convection and surface moisture flux/convection, so that the model cannot rest at a particular position in the (RH_s, Γ_N) plane. Periodic or quasi-periodic behavior appears instead. The period of the low-frequency oscillation is the time for the model to complete one cycle.

5. Discussion and concluding remarks

Using a highly simplified radiative–convective model, we have extended the work by Hu and Randall (1994) and have shown that low-frequency oscillations can arise spontaneously in radiative–convective systems with active surface evaporation.

Periods of moisture accumulation are characterized by strong surface evaporation and weak convection. The duration of such periods is determined by how long it takes for surface moisture flux to raise the mixed-layer relative humidity to a high value while fighting against convective drying. While the atmosphere is moistening, its tendency to maintain a moist neutral lapse rate through convection, in particular the process

C1 in Fig. 11, enhances radiative cooling, because radiation always tends to relax the atmosphere toward a steep lapse rate (Manabe and Möller 1961). This is a positive feedback between the surface moisture flux and radiation, made possible by convection. This feedback later breaks when the relative humidity of the mixed layer is high enough to suppress the surface moisture flux. Radiation then becomes the dominant process. At this stage, moist convection changes its primary role from reducing the lapse rate to drying the atmosphere, in order to make a moisture change consistent with the lapse rate steepening due to radiation. Intense convection in this period is also supported by the positive feedback between precipitation and surface evaporation. The duration of this period is determined by the radiation relaxation as modified by convective coupling of moisture and temperature changes.

The radiative control of temperature leads to a relatively cool atmosphere with a steep lapse rate. Meanwhile, the mixed layer dries out after a period of intense convection. Convection weakens at the end of this period when the equivalent potential temperature in the mixed layer is minimized. The surface moisture flux then becomes the dominant process. Another period of moisture accumulation ensues and the whole process repeats.

Steady solutions are possible, depending on the parameters. However, as we showed in both the analytical and numerical analyses, these solutions occur only when the mixing ratio in the mixed layer is very close to that of the saturation mixing ratio at the given SST. The surface evaporation under these conditions is weak. Observations (e.g., Gray 1979) show, however, that the tropical atmospheric mixed layer is far from saturation. The surface moisture flux is indeed an active process in the Tropics.

The essential mechanism of the oscillations from both this model and the numerical models in Part I is the same. This mechanism is supported by many observations. An example is shown in Fig. 12, which presents the time sequences of perturbations of the surface pressure, RH_s, and Γ_N during a two-year period[1] at Truk Island (7.5N, 151.9E). A bandpass filter (Murakami 1979), centered at 40 days with a half-width of 10 days, was applied to the data before plotting. As shown in this result, RH_s and Γ_N vary in an out-of-phase relation. At high surface pressure, the surface relative humidity is low and the lapse rate is steep. The arrival of low surface pressure is accompanied by high surface relative humidity and a weak lapse rate. This filtered result also shows that the sum of the values of RH_s and Γ_N is very close to unity.

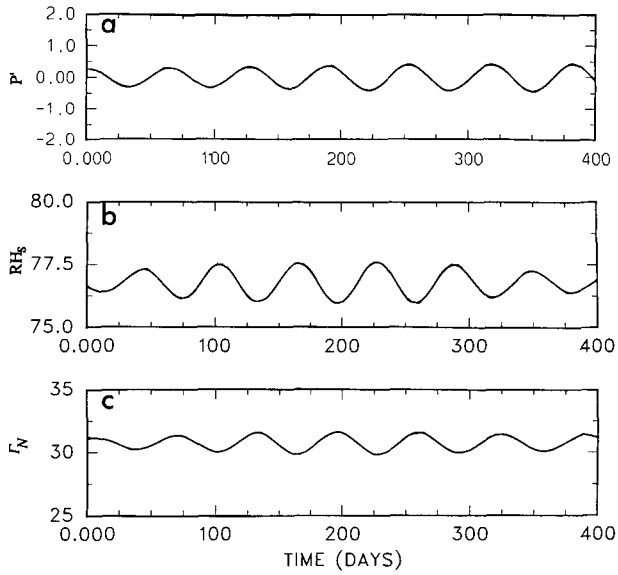

FIG. 12. Bandpass filtered perturbations of (a) the surface pressure (hPa), (b) the surface relative humidity (%), and (c) the normalized atmospheric lapse rate Γ_N (%) from the Truk data.

Although a direct application of our theory to the observed tropical low-frequency oscillations is limited because we have deliberately omitted dynamics and its interaction with convection in our models, our theory suggests partial explanations for many aspects of the observed oscillations. For example, it explains the 30–60 day oscillations in precipitation and convective heating source in the Tropics, as reported by Hartmann and Gross (1988) and Hsu et al. (1990). It also explains the observed oscillation of the surface moisture flux in the warm-water regions of the Indian and western Pacific Oceans (Krishnamurti et al. 1988).

For the tropical 30–60 day oscillations there is evidence (e.g., Hartmann and Gross 1988) that in the western Pacific the anomalies in convective precipitation, and therefore in the atmospheric heating, lead those in the motion field. This observation argues against wave–CISK theories of the 30–60 day oscillation. Our theory offers a plausible explanation for oscillations of the convection and latent heating over the warm oceans. It shows that the oscillations can occur without support from large-scale dynamics. As demonstrated by results from variety of numerical studies (e.g., Yamagata and Hayashi 1984; Salby and Garcia 1987; among others) a low-frequency oscillating heat source in the Tropics can drive tropical waves with vertical structures and phase speeds comparable to those of the observed 30–60 day oscillations. As such waves develop, they will inevitably interact with the convection.

Acknowledgments. We greatly appreciate the comments, suggestions, and stimulating discussions offered by Professors Duane Stevens (now at the University of

[1] The data start on 1 January 1984 and end on 31 December 1985. These two years were selected because there are no missing soundings.

Hawaii), Graeme Stephens and Wayne Schubert of Colorado State University, Dr. Klaus Weickmann of NOAA ERL, and Professor Chris Bretherton of University of Washington. We thank Professor Bill Gray of Colorado State University for providing us with the Truk data. Q. Hu also thanks Dr. Chris Walcek of SUNYA for encouragement.

We thank the anonymous reviewers for their comments that helped us to clarify some thoughts and led to improvement of the manuscript.

This research was sponsored by NASA under Grant NAG-5-1058, by the U.S. Department of Energy under Grant DE-FG02-89ER-69027, both through Colorado State University. While revising this manuscript, Q. Hu was supported by Air Force Office of Scientific Research under Grant F49620-92-J-0018 and by the U.S. Department of Energy under Grant DE-FG02-92ER61364, both through the State University of New York at Albany.

APPENDIX A

The Form of the Detrainment Terms in the Dry-Static Energy and Moisture Equations

The form of D in (8) is determined from the conservation of dry static energy in the atmospheric column (Schubert 1974):

$$\frac{\partial}{\partial t}\int_{p_T}^{p_0} s(p,t)\frac{dp}{g} = F_{s_0} + LP_r + \int_{p_T}^{p_0} Q_R\frac{dp}{g}. \quad \text{(A1)}$$

The left-hand side of (A1), after substitution from (8) and (12) and use of the assumption that p_T, p_B, and p_0 are constants, becomes

$$\frac{\partial}{\partial t}\int_{p_T}^{p_0} s(p,t)\frac{dp}{g} = F_{s_0} + \int_{p_T}^{p_0} Q_R\frac{dp}{g} + Lq_M M_c - D\frac{p_B - p_T}{g}. \quad \text{(A2)}$$

Comparison of the terms on the right-hand side of (A1) and (A2) yields

$$D = \frac{gL}{p_B - p_T}(q_M M_c + P_r).$$

Using the definition for precipitation, that is, (11), we have

$$D = g\frac{(1-c)Lq_M M_c}{p_B - p_T}. \quad \text{(A3)}$$

The detrainment term of (13) is determined from the conservation of total moisture; that is,

$$\frac{\partial}{\partial t}\int_{p_T}^{p_0} q(p,t)\frac{dp}{g} = F_{q_0} - P_r. \quad \text{(A4)}$$

With the use of (11), (13), and (14), (A4) yields

$$\begin{aligned}\frac{\partial}{\partial t}\int_{p_T}^{p_0} q(p,t)\frac{dp}{g} &= \frac{\partial}{\partial t}\left[\int_{p_T}^{p_B} q(p,t)\frac{dp}{g} + \int_{p_B}^{p_0} q(p,t)\frac{dp}{g}\right] \\ &= -q_{B^+}M_c + q_T M_c + M_c K P_q[1 - e^{(p_T - p_B/P_q)}] \\ &\quad + F_{q_0} - M_c(q_M - q_{B^+}) \\ &\approx F_{q_0} + M_c(KP_q - q_M). \quad \text{(A5)}\end{aligned}$$

Here $\exp[P_q^{-1}(p_T - p_B)] \ll 1$ was used. Comparison of the terms on the right-hand sides of (A4) and (A5) yields

$$K = \frac{(1-c)}{P_q}q_M. \quad \text{(A6)}$$

APPENDIX B

Symbols in Eq. (22)

$$A = \frac{gv}{\Delta p_M} + \frac{1}{\tau} + \frac{g\bar{M}_c}{\Delta p_M}, \quad B = \frac{gv}{\Delta p_M}s_{00} + \frac{s_{R_M}}{\tau},$$

$$C = \frac{g\bar{M}_c}{\Delta p_M}, \quad D = \frac{g\bar{M}_c}{p_B - p_T},$$

$$F = \frac{g(1-c)\bar{M}_c}{p_B - p_T}, \quad H = 1 + \frac{c}{v}\bar{M}_c,$$

and

$$v = \rho_0 c_D |V_s|.$$

APPENDIX C

Solution for $\bar{M}_c$

For a neutral atmosphere, $G = 0$ or, equivalently,

$$(1-R)\bar{s}_M - (1-R)\bar{s}_{B^+} + (W - LR)\bar{q}_M = 0. \quad \text{(C1)}$$

Substituting (25) into the above we can get

$$(1-R)\frac{B}{A} - (1-R)\left(1 - \frac{C}{A}\right)\left(\frac{1}{\tau} + D - \frac{CD}{A}\right)^{-1} \times \left[\frac{\mathrm{BD}}{\mathrm{A}} + \frac{s_{R_B}}{\tau} + \mathrm{Lq}_{00}^{*}\left(\frac{\mathrm{D}-\mathrm{F}}{\mathrm{H}}\right)\right] + (W - LR)\frac{q_{00}^{*}}{H} = 0, \quad \text{(C2)}$$

where the symbols listed in appendix B were used. After some manipulations, (C2) can be rewritten as

$$A^2\left\{\frac{BH}{\tau} + (C-A)\left[H\frac{s_{R_B}}{\tau} + Lq_{00}^{*}(D-F)\right] + q_{00}^{*}\frac{(W-LR)}{(1-R)}\left[\frac{A}{\tau} + D(A-C)\right]\right\} = 0. \quad \text{(C3)}$$

As A, C, D, F, and H are all functions of $\bar{M}_c$, (C3) is a fourth-degree polynomial equation for $\bar{M}_c$. Two of the four solutions can be obtained from $A^2 = 0$. These two solutions give negative $\bar{M}_c$s, however, and fail to satisfy (21). The other two solutions can be obtained by setting the expression in { } equal to zero. It is straightforward, though tedious, to show that one of these two solutions is $\bar{M}_c \equiv 0$ and the other, which satisfies (21) for the given parameters listed in Table 1, has the form given in (23).

REFERENCES

Arakawa, A., and W. H. Schubert, 1974: Interaction of a cumulus cloud ensemble with the large scale environment: Part I. *J. Atmos. Sci.*, **31,** 674–701.

——, and J.-M. Chen, 1987: Closure assumptions in the cumulus parameterization problem. *Proc. WMO/IUGG NWP Symp.*, Tokyo, Japan, 107–131.

Betts, A. K., and W. Ridgway, 1989: Climate equilibrium of the atmospheric convective boundary layer over a tropical ocean. *J. Atmos. Sci.*, **46,** 2621–2641.

Gray, W. M., 1979: Hurricanes: Their formation, structure and likely role in the tropical circulation. *Meteorology over the Tropical Oceans,* D. B. Shaw, Ed., Royal Meteorological Society, 156–218.

Hartmann, D. L., and J. R. Gross, 1988: Seasonal variability of the 40–50 day oscillation in wind and rainfall in the tropics. *J. Atmos. Sci.*, **45,** 2680–2702.

Hsu, H.-H., B. J. Hoskins, and F. Jin, 1990: The 1985/86 intraseasonal oscillation and the role of the extratropics. *J. Atmos. Sci.*, **47,** 823–839.

Hu, Q., 1992: Low frequency oscillations in radiative–convective models. Ph.D. thesis, Colorado State University, 196 pp.

——, and D. A. Randall, 1994: Low-frequency oscillations in radiative–convective systems. *J. Atmos. Sci.*, **51,** 1089–1099.

Krishnamurti, T. N., D. K. Oosterhof, and A. V. Mehta, 1988: Air–sea interaction on the time scale of 30–60 days. *J. Atmos. Sci.*, **45,** 1304–1322.

Manabe, S., and F. Möller, 1961: On the radiative equilibrium and heat balance of the atmosphere. *Mon. Wea. Rev.*, **89,** 503–532.

Murakami, M., 1979: Large-scale aspects of deep convective activity over the GATE area. *Mon. Wea. Rev.*, **107,** 994–1013.

Paltridge, G. W., and C. M. R. Platt, 1976: *Radiative Processes in Meteorology and Climatology.* Elsevier, 318 pp.

Salby, M. L., and R. R. Garcia, 1987: Transient response to localized episodic heating in the tropics. Part I: Excitation and short-time near-field behavior. *J. Atmos. Sci.*, **44,** 458–498.

Satoh, M., and Y. Y. Hayashi, 1992: Simple cumulus models in one-dimensional radiative convective equilibrium problems. *J. Atmos. Sci.*, **49,** 1202–1220.

Schubert, W. H., 1974: Cumulus parameterization theory in terms of feedback and control. Atmos. Sci. Paper No. 226, Colorado State University, Fort Collins, 19 pp.

Waliser, D. E., and N. E. Graham, 1993: A comparison of the highly reflective cloud and outgoing longwave radiation datasets for use in estimating tropical deep convection. *J. Climate,* **6,** 331–353.

Yamagata, T., and Y. Hayashi, 1984: A simple diagnostic model for the 30–50 day oscillation in the tropics. *J. Meteor. Soc. Japan,* **62,** 709–717.